

# **HiSST: 4th International Conference on High-Speed Vehicle Science Technology**

22 -26 September 2025, Tours, France



# Topology optimization of engine cooling plate subjected to heterogeneous and distributed heat sources

Li Yu<sup>1,2</sup>, Linxin Tian<sup>3</sup>, Xinlei Li<sup>4</sup>, Kun Wu<sup>1,\*</sup>, Xuejun Fan<sup>1,2</sup>

#### Abstract

For the propulsion system of high-speed vehicles, an efficient thermal protection system is of great importance to ensure their safety and stability during flight. In this paper, the fuel cooling structure of the device installation panel for a combined-cycle engine is optimized using topology optimization method (TO) incorporating conjugate heat transfer. The topology optimization model employs a pseudo-density approach and takes the average temperature of the design domain as the optimization objective, while considering the material volume and power dissipation constraints. The optimizations were performed within a continuous adjoint framework implemented in OpenFOAM and reasonable optimized layouts were obtained. The optimized layouts are then extracted and further conjugate heat transfer simulations are performed. The results show that the optimized cooling structure has improved heat transfer performance compared to the conventional cooling structure and exhibits good performance under wide operating conditions.

Keywords: Topology optimization; Conjugate heat transfer; Cooling plate; Heat transfer performance

## **Nomenclature**

Latin

R – NS equation with the energy equation

u – Velocity

p – Pressure

T – Temperature

F - Artificial damping force

h – Enthalpy

 $Pr_t$  - Turbulence Prandtl number

Q - Volumetric heat source

V – Volume

**G** – Constraint function

 $R_{min}$  – Filtering radius

L – Lagrangian function

 $Q_s$  – Volumetric flow rate

 $\dot{m}$  – Mass flow rate

 $T_{\delta}$  – Temperature nonuniformity

 $R_{th}$  – Thermal resistance Da – Darcy number

l – Characteristic length scale

d - Pipe length

Greek

w - State variable

γ – Design variable

 $\rho$  – Density

 $\tau$  – Viscous strain

 $\lambda(\gamma)$  – Thermal conductivity

 $C_n(\gamma)$  – Heat capacity

 $\mu$  – Dynamic viscosity

 $\mu_t$  – Turbulent viscosity

 $\nu$  – Kinematic viscosity

 $\alpha$  – Interpolation function

 $\theta$  – Shape parameter

 $\Psi$  – Objective function

 $\varphi_{power}$  – Power dissipation constraint

 $V_{fluid}$  – Volumetric fraction constraint

λ – Adjoint variable

 $\beta$  – shape factors

 $\eta$  – shape factors

Page | 1

<sup>&</sup>lt;sup>1</sup>Institute of Mechanics, Chinese Academy of Sciences, Beijing 100190, China.

<sup>&</sup>lt;sup>2</sup>School of Engineering Sciences, University of Chinese Academy of Sciences, Beijing 100049, China.

<sup>&</sup>lt;sup>3</sup>School of Energy and Power Engineering, Nanjing University of Science and Technology, Nanjing, China.

<sup>&</sup>lt;sup>4</sup>Beijing Institute of Space Long March Vehicle, Beijing 100076, China.

<sup>\*</sup> Corresponding author: wukun@imech.ac.cn

## 1. Introduction

Hypersonic vehicles are long-range cruising vehicles that travel at speeds above Mach 5 in or across the atmosphere, whose main propulsion systems are supersonic combustion ramjet engines 1. During the flight, the engine endures extreme high temperature caused by aerodynamic heating and fuel combustion heat release, and the excessive heat flux will cause material failure and structure damage, thus the thermal protection system (TPS) is crucial for safe operating and flight performance.

Thermal protection systems can be categorized as passive thermal protection, semi-passive thermal protection, and active thermal protection 2, with active thermal protection being more effective from a long-term and reusable perspective. Active thermal protection includes regenerative cooling 4, film cooling 5, transpiration cooling 6, and convective cooling 7, among which liquid convective cooling is widely used in various fields due to its high efficiency and low cost. Liquid convection cooling leverages convective heat transfer between the coolant and the engine hot structures to take away heat, and its core is the design of the cooling configurations. At present, the main design methods are conventional optimization (straight-through channel, S-type, and U-type), bionic optimization 8 and topology optimization 9.

As shown in Fig 1, for an air-breathing combined cycle engine, a near-circular heterogeneous cooling plate is installed to cool down various electronic components of the engine. The main goal is to design the cooling channels for this complex configuration under the distributed heterogeneous heat sources. Conventional optimization and bionic optimization due to their design limitations 10 are not applicable for the design of cooling channels for this complex configuration. Topology optimization is a high degree-of-freedom [9] design method that is not constrained by the structure and the designer's experience, can provide greater design flexibility 11. And with the maturity of 3D printing technology, it has been gradually applied in various fields 12.

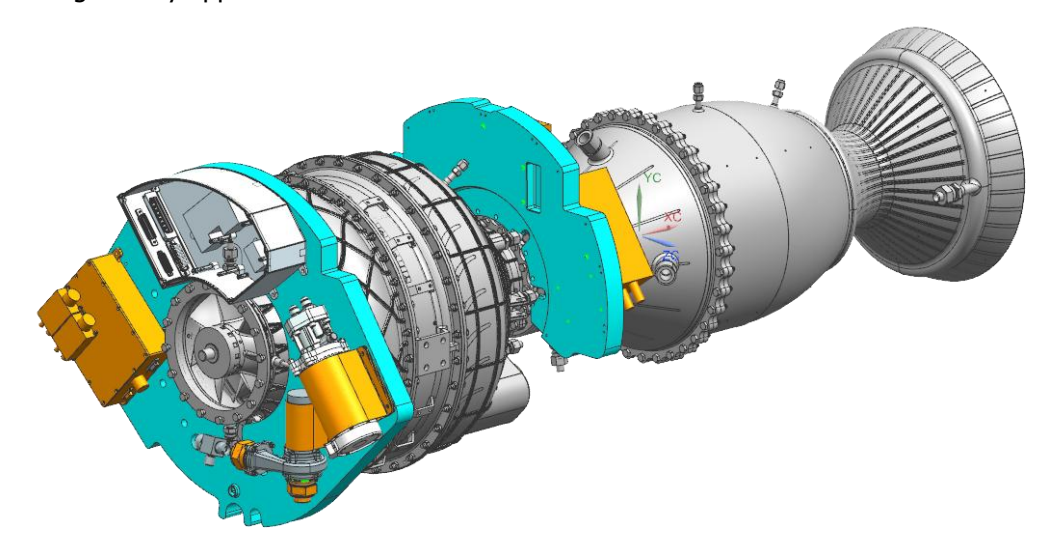


**Fig 1.** The assembly of the air-breathing combined cycle engine to show the functional of the cooling plate

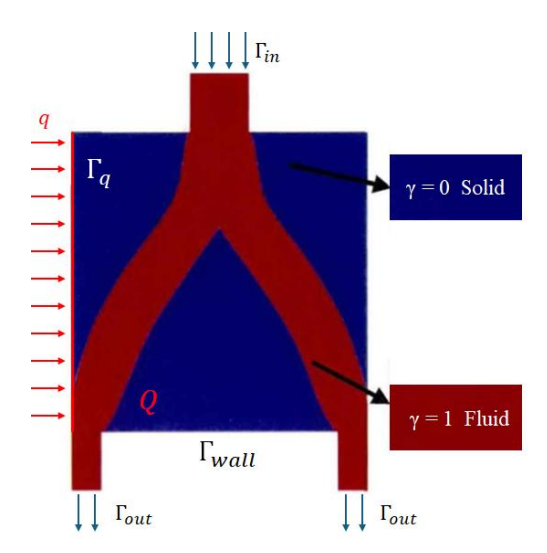


Fig 2. Schematic of the topology optimization

In this study, a simplified design domain is established based on the engine cooling plate, and distributed heat sources are imposed according to the actual heat source distribution of the engine. Subsequently, a topology optimization method developed in OpenFOAM is utilized to optimize the layout of this design domain. After obtaining a reasonable optimized configuration, the cooling channels' geometric structures are reconstructed and compared against the conventional design using the conjugate heat transfer simulation method under different operating conditions.

# 2. Methodology

Fig 2 illustrates a schematic of the topology optimization (TO) design for a coupled fluid-thermal problem, employing the pseudo-density method. The design domain is subjected to thermal loads from the external surface heat fluxes or internal volumetric heat sources. Heat exchanges between the fluid and solid phases as the coolant flows through the design domain, eventually reaching thermal equilibrium. The objective of the topology optimization is to determine the optimal spatial distribution of fluid-solid materials seeking for desired objective function, subject to various constraints.

#### 2.1. Optimization model

Firstly, a coupled fluid-thermal topology optimization model is established, which is governed by the following compressible, steady-state Navier-Stokes equation along with the energy equation:

$$R(\boldsymbol{w}, \gamma) = \left(R_{p}, R_{\boldsymbol{u}}, R_{T}\right)^{\mathrm{T}} = \begin{cases} -\nabla \cdot (\rho \boldsymbol{u}) \\ \nabla \cdot (\rho \boldsymbol{u} \boldsymbol{u}) - \nabla \cdot \boldsymbol{\tau} + \nabla p - \boldsymbol{F} \end{cases}$$

$$\left\{\nabla \cdot \left[\rho \boldsymbol{u} \left(h + \frac{1}{2} \boldsymbol{u} \cdot \boldsymbol{u}\right)\right] - \nabla \cdot \left[\left(\frac{\lambda(\gamma)}{C_{p}(\gamma)} + \frac{\mu_{t}}{Pr_{t}}\right) \nabla h\right] - \nabla \cdot (\boldsymbol{\tau} \cdot \boldsymbol{u}) - Q \right\}$$

$$(1)$$

where  ${\bf u}$  and p respectively denotes the velocity and pressure.  $\rho$ ,  $C_p$ ,  $\mu$ ,  $\lambda$ , Q and h respectively represent density, specific heat capacity, dynamic viscosity, thermal conductivity, volumetric heat source and specific enthalpy. The viscous strain  ${\bf \tau}$  is defined as  ${\bf \tau}=2\mu_{\rm eff}S({\bf u})=\mu_{\rm eff}(\nabla {\bf u}+\nabla {\bf u}^{\rm T})$ ,  $\mu_{\rm eff}$  is the effective viscosity, which includes the viscosity from both laminar and turbulent perspectives.

In contrast to the standard Navier-Stokes equations, this model for optimization incorporates an artificial damping force, F, within its momentum equation. This modification allows for the macroscopic simulation of the flow as a single-term porous media flow 15:

$$\mathbf{F} = -\alpha(\mathbf{v})\mathbf{u} \tag{2}$$

$$\alpha(\gamma) = \alpha_{\text{max}} \frac{\theta(1-\gamma)}{\theta+\gamma} \tag{3}$$

where  $\gamma$  is the design variable (known as pseudo-density), and  $\alpha_{\rm max}$  is a relatively large number to provide effective resistance when  $\gamma$  reaches 0, and  $\theta$  represents the shape parameter. The shape of the interpolation function could be seen in Fig 3. Different from the homogeneous porous media, the permeability in the TO layouts change locally by using the interpolation function.

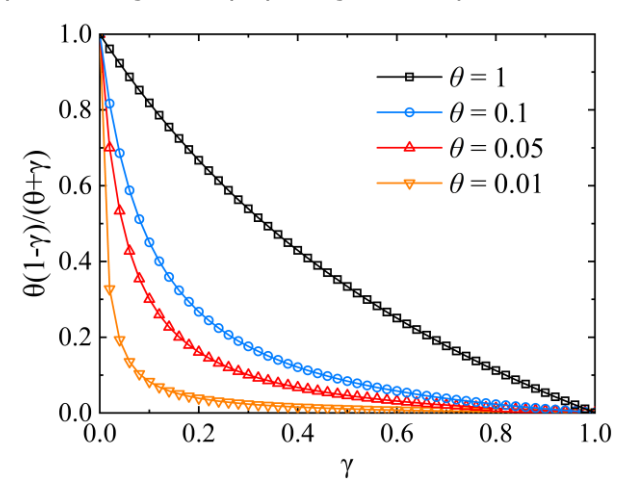


**Fig 3.** Interpolation function with different shape parameter  $\theta$ 

The determination of  $\alpha_{\rm max}$  is the most important task during the optimization process. For most applications regarding to the topology optimization of the fluid flow and heat transfer problems,  $\alpha_{\rm max}$  is defined as  $\alpha_{\rm max} = \frac{\mu}{Da \cdot l^2}$ , where Da is the Darcy number and l is the characteristic length scale. The Da serves as an indicator of the fluid permeability within the porous medium. A higher Da value implies a smaller  $\alpha_{\rm max}$ , signifying that the volumetric force is inadequate to effectively constrain the flow field. Conversely, excessively low Da values can result in an overly stiff source term, which adversely affects the solution of the momentum equation. Olesen et al. 15 have proposed that a Da value of  $10^{-5}$  or less is suitable. Moreover, a small initial value is typically assigned to  $\alpha$ , which is successively increased to  $\alpha_{\rm max}$  during the optimization process. Subsequently, interpolation of coefficients  $\lambda$  and  $C_p$  within the energy equation is also required:

$$\lambda(\gamma) = \lambda_{fluid} + (\lambda_{solid} - \lambda_{fluid}) \frac{\theta(1 - \gamma)}{\theta + \gamma}$$
(4)

$$C_{p}(\gamma) = C_{p\_fluid} + (C_{p\_solid} - C_{p\_fluid}) \frac{\theta(1 - \gamma)}{\theta + \gamma}$$
(5)

In addition to the governing equations described above, the minimum average temperature of the design domain is defined as the objective function, denoted as  $\psi$ . Two inequality constraints are imposed: the power dissipation constraint  $\varphi_{power}$  and the volumetric fraction constraint of fluid  $V_{fluid}$ . These are as follows:

$$\Psi = \frac{1}{V} \int_{\Omega} T \, d\Omega \tag{6}$$

$$\varphi_{power} = -\int_{\Gamma} (p + \frac{1}{2}\rho \mathbf{u}^2) \mathbf{u} \cdot \mathbf{n} \, d\Gamma \tag{7}$$

$$V_{fluid} = \frac{1}{V} \int_{\Omega} \gamma \, d\Omega \tag{8}$$

In summary, a complete density-based topological optimization method can be described as follows:

$$G(\mathbf{w}, \gamma) = (g_{\text{vol}}, g_{\text{power}})^{T} = \begin{cases} V_{\text{fluid}} - V_{\text{max}} \\ \varphi_{\text{power}} - \varphi_{\text{max}} \end{cases}$$
(9)

$$\begin{cases} Find: & \gamma \\ Minimize: & \Psi(\mathbf{w}, \gamma) \\ Subject to: & \mathbf{R}(\mathbf{w}, \gamma) = 0 \\ & \mathbf{G}(\mathbf{w}, \gamma) \leq 0 \\ & 0 \leq \gamma \leq 1 \end{cases}$$
 (10)

#### 2.2. Sensitivity analysis and numerical processing

This paper employs the Method of Moving Asymptotes (MMA) to solve the multi-objective optimization problem, as its iterative process is relatively stable, making it an ideal choice for large-scale engineering optimization problems 17. To obtain the gradient of the objective function, we used the continuous adjoint method for the solution 18. First, we establish a Lagrangian function in the following form:

$$L = \Psi + \int_{\Omega} \lambda \cdot R(\mathbf{w}; \gamma) \, d\Omega = \Psi + \langle \lambda, R(\mathbf{w}; \gamma) \rangle$$
 (11)

Among them,  $\lambda = (p_a, u_a, T_a)$  is the lagrangian multiplier, also known as the adjoint variable. Since  $R(w; \gamma) = 0$ , the sensitivity of the original objective function with respect to the design variables is equivalent to the total derivative of the following Lagrangian function:

$$\frac{dL}{dv} = \frac{\partial \psi}{\partial v} + \frac{\partial \Psi}{\partial w} \frac{dw}{dv} + \frac{\partial \langle \lambda, R \rangle}{\partial v} + \frac{\partial \langle \lambda, R \rangle}{\partial v} \frac{dw}{dv} = \frac{\partial \psi}{\partial v} + \frac{\partial \langle \lambda, R \rangle}{\partial v} + (\frac{\partial \Psi}{\partial w} + \frac{\partial \langle \lambda, R \rangle}{\partial w}) \frac{dw}{dv}$$
(12)

Based on the idea of the adjoint method, we set the adjoint variable to satisfy the following equation:

$$\frac{\partial \Psi}{\partial \boldsymbol{w}} + \frac{\partial \langle \boldsymbol{\lambda}, \boldsymbol{R} \rangle}{\partial \boldsymbol{w}} = \begin{cases}
\frac{\partial \Psi}{\partial p} + \frac{\partial \langle p_a, R_p \rangle}{\partial p} + \frac{\partial \langle \boldsymbol{u}_a, \boldsymbol{R}_u \rangle}{\partial p} + \frac{\partial \langle T_a, R_T \rangle}{\partial p} = 0 \\
\frac{\partial \Psi}{\partial \boldsymbol{u}} + \frac{\partial \langle p_a, R_p \rangle}{\partial \boldsymbol{u}} + \frac{\partial \langle \boldsymbol{u}_a, \boldsymbol{R}_u \rangle}{\partial \boldsymbol{u}} + \frac{\partial \langle T_a, R_T \rangle}{\partial \boldsymbol{u}} = 0 \\
\frac{\partial \Psi}{\partial T} + \frac{\partial \langle p_a, R_p \rangle}{\partial T} + \frac{\partial \langle \boldsymbol{u}_a, \boldsymbol{R}_u \rangle}{\partial T} + \frac{\partial \langle \boldsymbol{u}_a, \boldsymbol{R}_T \rangle}{\partial T} = 0
\end{cases} \tag{13}$$

By simplifying the above system of equations using integral transforms, we can obtain the control equations required to solve for the adjoint variables. Correspondingly, the total derivative of the Lagrange function, i.e., the sensitivity of the original objective function, is converted into the following form in Eqn. (14). After solving for the original state variables and adjoint variables, we can calculate the value of this sensitivity. Then a gradient-based optimization algorithms MMA (the Method of Moving Asymptotes) is utilized as the optimizer to obtain the updated design variable  $\gamma$ .

$$\frac{\mathrm{d}L}{\mathrm{d}\gamma} = \frac{\partial \Psi}{\partial \gamma} + \frac{\partial \langle \lambda, R \rangle}{\partial \gamma} \tag{14}$$

Since the topology optimization model uses the pseudo-density method, it is prone to producing unrealistic layouts during the optimization process, such as mesh-dependencies layouts and checkerboard pattern, which severely affect the material layout and solution convergence 19. Previous researches show that some filtering approach can effectively solve the above problems. Therefore, this paper uses Helmholtz partial differential equations as the filter 20, whose equation is as follows:

$$\gamma_f = R_{min}^2 \nabla^2 \gamma_f + \gamma \tag{15}$$

where  $\gamma$  is the pseudo-density before filtering,  $\gamma_f$  is the pseudo-density after filtering, and  $R_{min}$  is the filtering radius. In addition, filtering may produce gray-scale element ( $\gamma$  is between 0 and 1). To solve this problem, a projection function can be used to obtain a clear fluid-solid boundary. In this paper, the following hyperbolic tangent function 21 is used to project  $\gamma_f$ :

$$\gamma_p = \frac{\tanh(\beta\eta) + \tanh(\beta(\gamma_f - \eta))}{\tanh(\beta\eta) + \tanh(\beta(1 - \eta))}$$
(16)

In the above equation,  $\gamma_p$  is the projected pseudo-density, and  $\beta$  and  $\eta$  are shape factors that control the shape of the projection function. Finally, a complete TO solver is constructed on OpenFOAM, and the schematic of the topology optimization process is shown in Fig 4.

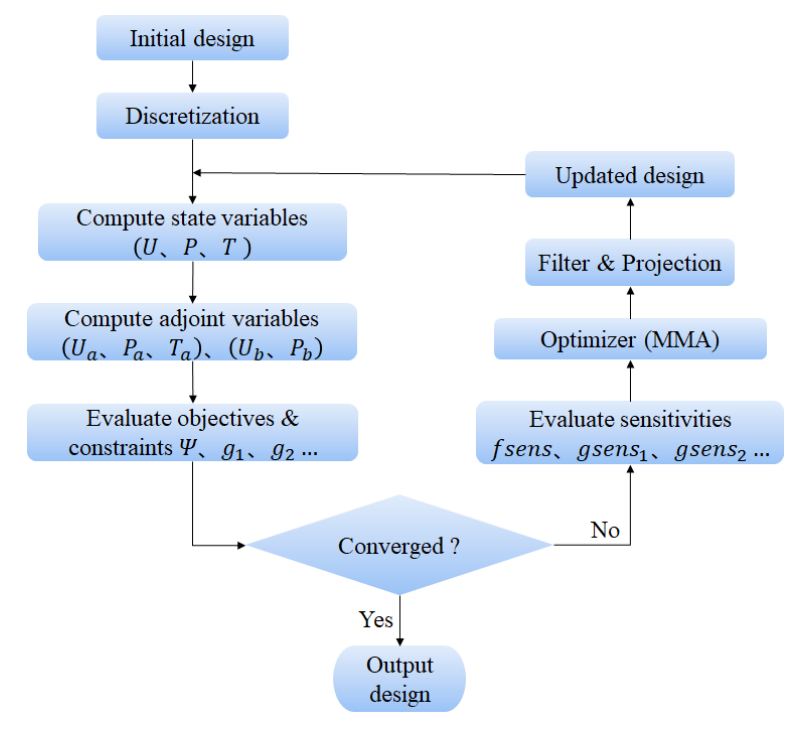


**Fig 4.** Schematic of the topology optimization process.

## 3. Results and discussions

#### 3.1. Topology optimization layouts

The structural schematic and heat source distribution of the design domain are presented in Fig 5, which is a scale-down version of the original structure as in Fig 1, with a characteristic dimension L=2 mm. The salient feature of the present cooling plate lies in that it is subjected to heterogeneous and distributed heat sources. The radiation heat load from the engine combustor is modelled by a uniform heat flux as denoted in region  $q_I=1.6\times 10^4$  W/m². Regions II and V are exposed to heat generation from two electronic devices, wherein  $q_{II}=7.1\times 10^4$  W/m² and  $q_V=5.2\times 10^4$  W/m². Additionally, two solenoid valves also need heat dissipation, whose heat generation powers are  $q_{III}=q_{IV}=9.1\times 10^5$  W/m². For the standard design condition, coolant is dodecane at room temperature (300K) with its mass flow rate being  $\dot{m}_{in}=0.3$  g/s, while the operating pressure is set to 3 MPa which is relatively higher than its supercritical pressure. Based on the above operating conditions, a series of optimizations were performed to minimize the domain-averaged temperature, subject to a flow power dissipation constraint of 0.00011 and a volumetric fraction constraint of 0.55. The specific optimization parameters are shown in Table 1.

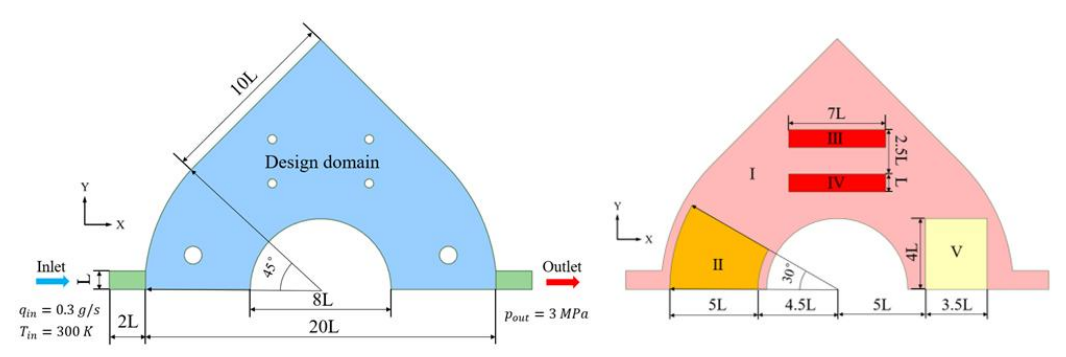


**Fig 5.** (a) Geometry size (b) Heat source distribution.

Parameter	Value	Parameter	Value
$\dot{m}_{in}$	0.3 g/s	$q_V$	52 kW/m <sup>2</sup>
$T_{out}$	300 K	$lpha_{ ext{max \_}initial}$	229
$p_{out}$	3 MPa	$\alpha_{ ext{max }\_end}$	3e7
$q_I$	16 kW/m <sup>2</sup>	$V_{\max}$	0.55
$q_{II}$	71 kW/m <sup>2</sup>	$arphi_{ ext{max}}$	1.1e-4
$q_{III}, q_{IV}$	910 kW/m <sup>2</sup>	$\theta$	0.01

**Table 1.** Parametric settings used for the TO model

Fig 6(a) illustrates a representative of the optimal configuration layout. To validate the heat transfer performance of the topology optimization configuration, a comparative analysis is conducted between the topology optimized (TO) configuration and a straight-channel heat sink (SC) configuration, with the SC structure demonstrated in Fig 6(b). We note that the SC configuration owns the same structural volume ratio to make it comparable to the TO configuration. Correspondingly, the TO configuration is extracted by the region of  $\gamma < 0.5$  in the TO field. A three-dimensional conjugate heat transfer (CHT) solver is employed for the numerical simulations, in which the coolant channel height is set to 2 mm and the upper and lower plate thicknesses are 0.75 mm. Subsequently, both configurations are discretized using unstructured tetrahedral meshes. Through a grid independence study, the mesh grids for both configurations are determined to be approximately 10 million elements, and prism layers are generated near the coupling surfaces between the fluid and solid domains. The first cell size in the boundary layer is 2  $\mu$ m to ensure that the dimensionless wall distance y+ below 5, and the grids near the leading and trailing edges of the solid cells are refined. The meshing of the TO configuration is shown in Fig 7.

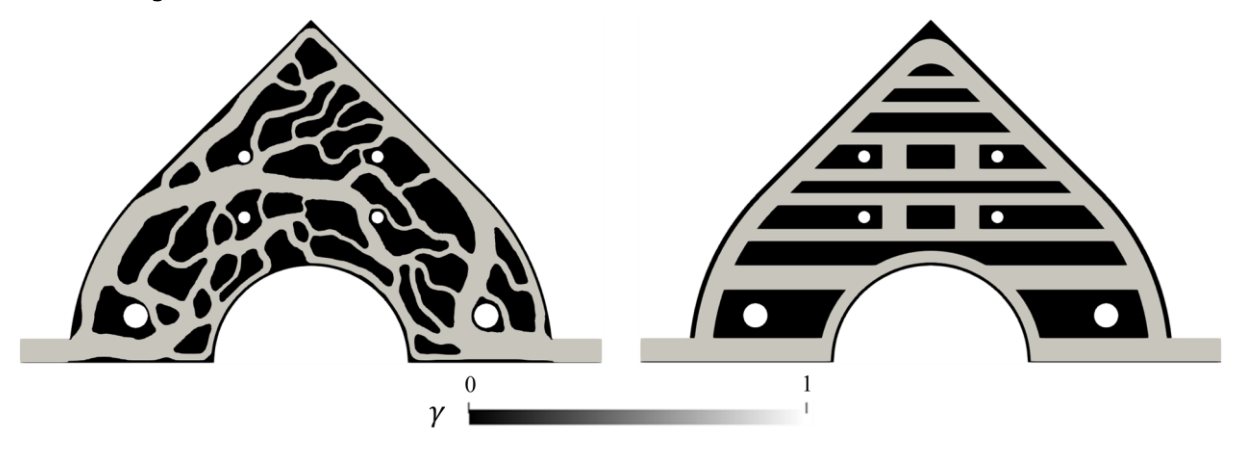


Fig 6. (a) Topology optimized configuration (b) Straight-channel configuration

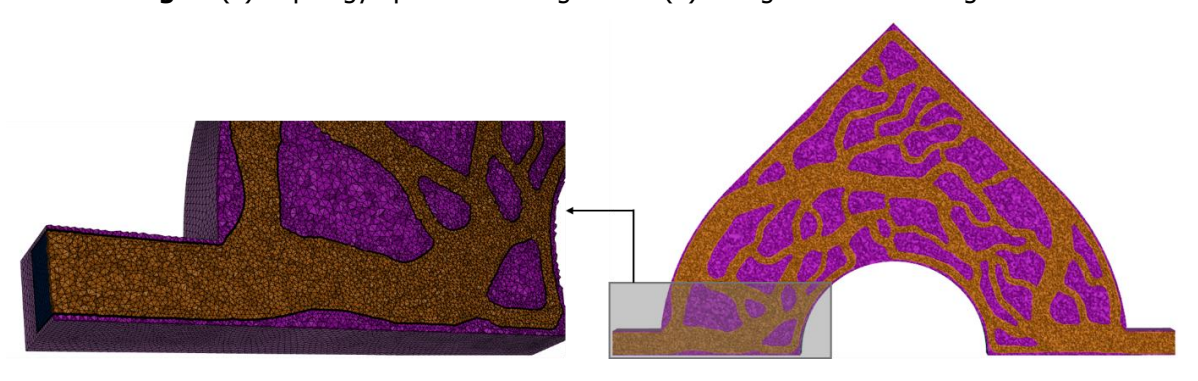


Fig 7. Mesh details of the TO cooling plate

#### 3.2. Conjugate heat transfer assessment

Fig 8 presents the temperature contours of the heating surface, the temperature and velocity contours of the central plane for both the TO and SC configurations. As shown in Fig 8(a), the temperature distributions on the heating surfaces of the two cooling plates exhibit overall consistency. Owing to the influence of solenoid valves, high-temperature regions are concentrated in the two central rectangular zones, with a remarkable temperature gradient relative to the inlet section. Nevertheless, the maximum temperature in the TO configuration is markedly lower than that of the SC configuration, thereby alleviating the thermal load at the center of the cooling plate. Furthermore, the TO channel demonstrates a more uniform temperature distribution under heat sources II and V, suggesting its superior capability in managing complex heat source conditions.

Temperature and velocity contours in the central plane are shown in Fig 8(b) and (c). In both the TO and SC configurations, the inlet flow impinges on the wall and bifurcates into two primary streams—an upward stream and a downward stream—which are subsequently distributed into smaller channels. For the downward stream, the SC configuration design prevents effective utilization of this portion of the coolant. After passing beneath the cooling plate, most of the coolant continues directly towards the outlet, with only a limited fraction diverted into the surrounding channels. In the TO configuration, the rapid contraction of the flow passage accelerates the coolant towards the central solenoid valves region and generates multiple intricate sub-channels, which facilitates uniform coolant distribution across the cooling plate. In contrast, in the SC configuration, the upward stream of the coolant is sequentially delivered to all lateral flow channels. However, as the main flow rate diminishes, the velocity also decreases, leading to insufficient coolant supply to the lateral channels closer to the upper region in the whole domain. This results in non-uniform coolant distribution and exacerbates temperature inhomogeneity, particularly in the central solenoid valves region, where the temperature of the upper solid part is significantly higher than that of the lower part. In the TO configuration, only a small fraction of the coolant is directed above the cooling plate, while the majority of the flow is guided directly into the central solenoid valves region and then split at the pointed protrusion cell (indicated by the red arrow) to cool areas III and IV. On the one hand, this maximizes the utilization of the coolant to reduce the temperature in the high-heat-source region; on the other hand, the split channels experience varying degrees of contraction, which increases coolant velocity and thereby enhances heat transfer efficiency.

Further analysis of the velocity contours indicates that numerous recirculation zones of different scales are present in the SC configuration, particularly at the intersections of certain branches. In contrast, the manifold structure of the TO configuration effectively suppresses these recirculation zones, thereby reducing coolant energy dissipation. In the SC configuration, such recirculation not only diminishes local convective heat transfer but also induces thermal non-uniformities and promotes the formation of hot spots. By mitigating these effects, the TO configuration ensures more uniform coolant distribution, minimizes unnecessary energy losses, and ultimately enhances both cooling efficiency and system reliability.

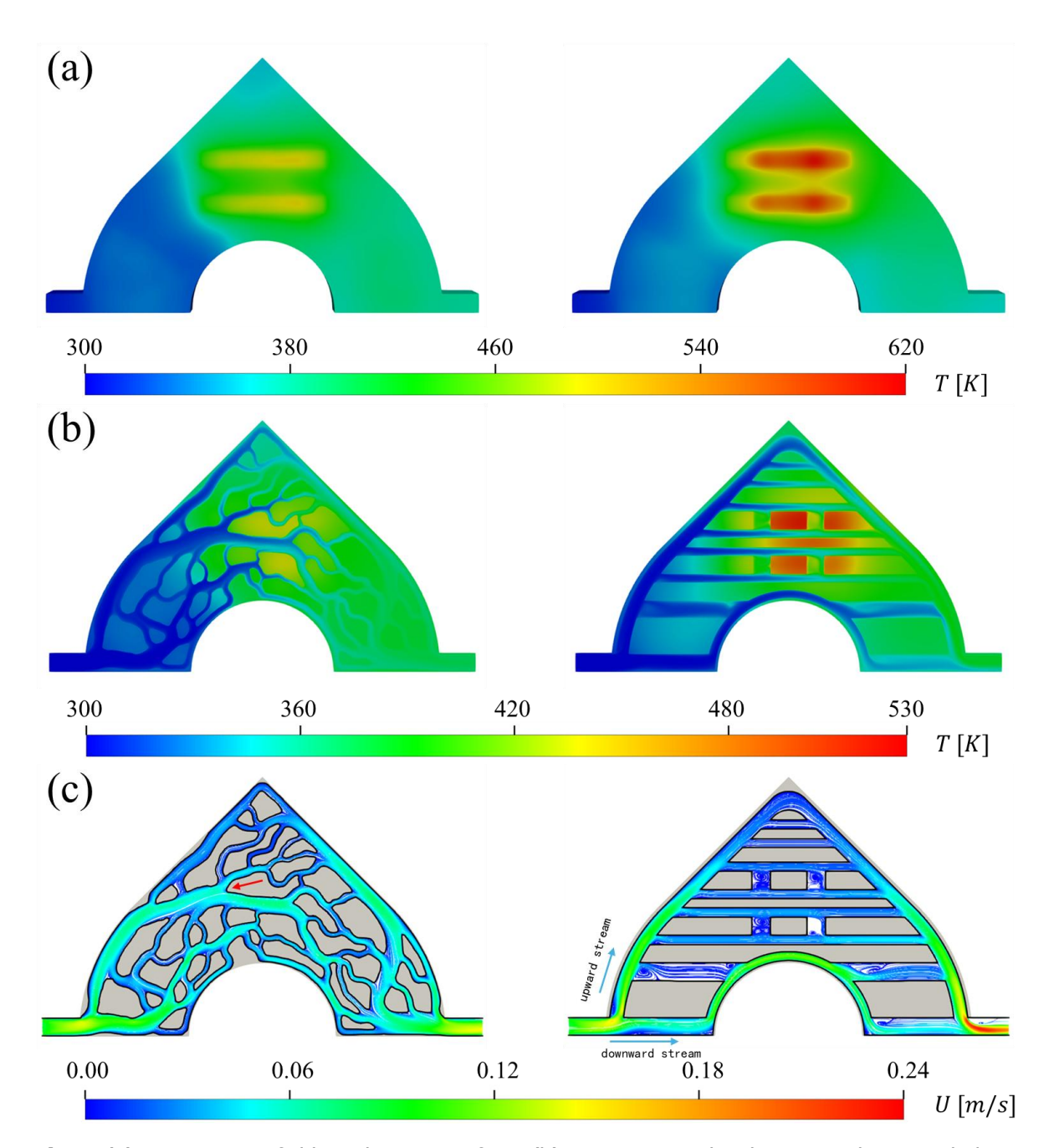


**Fig 8.** (a) Temperature fields on heating surface; (b) Temperature distribution on the central plane; (c) Velocity field on the central plane

Fig 9 displays the distribution of vortex structures with intensities exceeding  $75~\rm s^{-1}$  (rendered by velocity) in both configurations. The TO configuration exhibits a much richer vortex distribution compared with the SC configuration. In the SC configuration, vortices are primarily confined to the bends and junctions of the flow passages, and their scales are considerably smaller than those observed in the TO configuration. In the central solenoid valves region of the TO configuration, the combined effects of high-velocity coolant, solid structure disturbances, and the tortuous local surfaces generate vortices of various sizes that are nearly uniformly distributed throughout this region, thereby markedly enhancing local heat transfer. In contrast, the SC configuration develops larger vortices only at junctions, while the straight passages predominantly contain smaller vortical structures. Overall, the TO configuration demonstrates a superior capacity for heat exchange compared with the SC configuration, primarily due to the following factors: Firstly, the complex reticular flow channels of the TO configuration enlarge the fluid–solid contact area, thereby enhancing overall heat transfer performance; Secondly, the configurations geometry of the TO configuration accelerates the coolant flow, which

reduces boundary layer thickness and effectively strengthens convective heat transfer, while also mitigating local hot spots associated with convergence zones. Lastly, under the combined effects of increased coolant velocity and interactions with the complex cooling passage, coolant disturbance and mixing are intensified, leading to improved boundary-layer heat transfer and overall cooling performance.

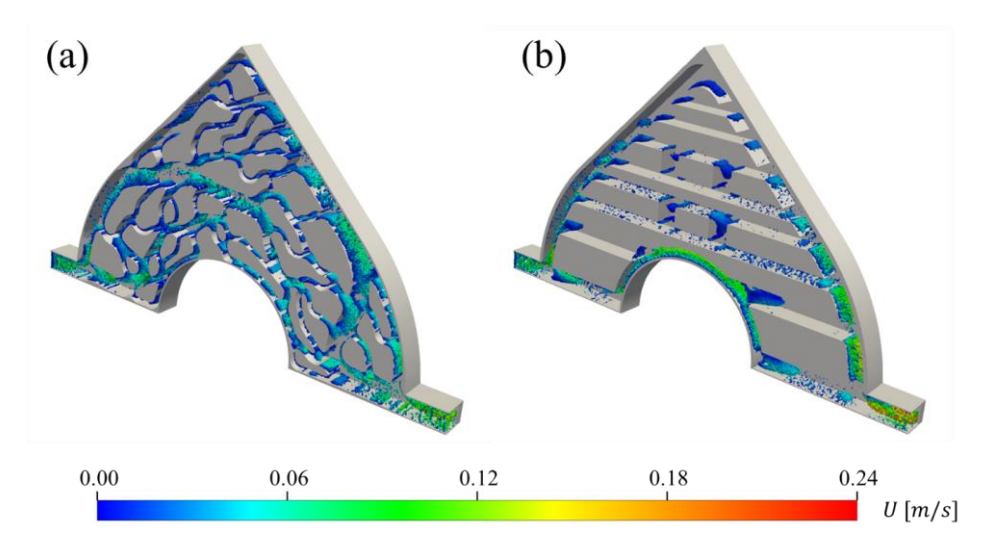


Fig 9. Vortex contour of TO and SC configurations

In practical applications, hypersonic vehicles are exposed to various extreme operating conditions, under which the thermal environment of the cooling plate also varies. To replicate these scenarios, three additional thermal load distributions are designed based on the actual operating modes of the hypersonic vehicles. These distributions primarily focus on the average heat source of the cooling plate (engine combustor) and the high heat source sizes in Zones III and IV (solenoid valves). The specific heat source distributions corresponding to different operating modes are summarized in Table 2.

Working Mode	$q_I$ [kW/m $^2$ ]	$q_{II}$ [W/m <sup>2</sup> ]	$q_{III}, q_{IV}$ [W/m <sup>2</sup> ]	$q_V$ [W/m $^2$ ]
Mode 1	16	71	910	52
Mode 2	40	71	910	52
Mode 3	10	71	1820	52
Mode 4	40	71	1820	52

**Table 2.** Operating conditions for TO configuration assessment

Fig 10 presents the temperature and velocity contours of the two cooling configurations under different working modes. The results indicate that their overall temperature distribution and coolant flow characteristics remain generally consistent. To further evaluate the comprehensive performance of the two configurations, the average coolant temperature  $T_{ave}$ , maximum coolant temperature  $T_{max}$ , and pressure drop  $\Delta p$  were extracted for comparison, as summarized in Table 3. In working mode 1, both the solenoid valves and the engine operate under normal conditions. At this stage, the average and maximum coolant temperatures in the cooling plate remain at relatively low levels. For the TO configuration, the values of parameters  $T_{ave}$ ,  $T_{max}$ , and  $\Delta p$  are 354.1 K, 512.6 K, and 36.8 Pa, respectively. In contrast, for the SC configuration, the corresponding values of  $T_{ave}$ ,  $T_{max}$ , and  $\Delta p$  are 363.1 K, 590.3 K, and 46.9 Pa, respectively. The TO configuration exhibits a 2.31% lower average coolant temperature ( $T_{ave}$ ), a 13.16% lower maximum temperature ( $T_{max}$ ) and a 21.54% lower pressure drop ( $T_{ave}$ ) compared to the PC configuration.

In working mode 2, the engine combustor operates under an overloaded condition, whereas in working mode 3, the solenoid valve becomes overloaded. As the thermal load intensifies in both scenarios, both the average and maximum coolant temperatures increase to varying degrees. Meanwhile, a slight decrease in pressure drop is observed, likely due to the temperature-induced reduction in coolant viscosity. Despite the harsher thermal conditions, the TO configuration consistently outperforms the SC

configuration across both modes—exhibiting lower average temperatures, reduced maximum temperatures, and smaller pressure drops. In working mode 2, the TO configuration achieves reductions of 2.63% in average temperature, 13.73% in maximum temperature, and 22.20% in pressure drop compared to the SC configuration; similarly, in mode 3, the reductions are 3.93%, 16.64%, and 24.36%, respectively. These improvements underscore the enhanced thermal management capability and flow efficiency of the TO configuration under localized high-load conditions. In working mode 4, both the engine and the solenoid valve are in an overloaded state, resulting in the most extreme thermal environment. Under these conditions, the average and maximum coolant temperatures reach their highest values. Correspondingly, the TO configuration outperforms the SC configuration, with reductions of up to 4.26% in average temperature, 17.01% in maximum temperature, and 25.10% in pressure drop. Based on the above results, it is evident that the performance advantage of the TO configuration over the SC configuration becomes more pronounced with increasing heat source intensity, underscoring its superior adaptability to complex thermal environments. Furthermore, the pressure drop in both configurations decreases slightly as the heat source strengthens. To explain this phenomenon, we draw an analogy with the Poiseuille law, as shown in the following equation:

$$\Delta p = \frac{128\mu L_C Q_s}{\pi d_C^4} \tag{17}$$

Where  $d_C$  represents the radius of the pipe,  $L_C$  is the length of pipe,  $\mu$  is the dynamic viscosity of the coolant, and  $Q_S$  is the volumetric flow rate of the coolant. Since the current numerical simulation uses a mass flow inlet, the above equation can be transformed as follows:

$$\Delta p = \frac{128\nu L_C \dot{m}}{\pi d_C^4} \tag{18}$$

Where  $\dot{m}$  represents the mass flow rate,  $\nu$  denotes the kinematic viscosity of the coolant. Since the cooling plate configuration remains unchanged, it can be assumed that  $L_c$  and  $d_c$  stay constant. Additionally, as this study uses a mass flow inlet,  $\dot{m}$  can also be considered constant. As the temperature increases, the kinematic viscosity of the coolant decreases, which in turn reduces the frictional resistance between fluid layers. This results in a decrease in flow resistance, leading to a reduction in pressure drop.

Fig 11 presents the heat transfer coefficients and temperature non-uniformity on the heating surface of the two configurations under different working modes. The temperature non-uniformity  $T_{\delta}$  is quantified using the following formula:

$$T_{\delta} = \frac{\int_{A_c} (T - T_{avg})^2 dA_c}{\int_{A_c} dA_c}$$
 (19)

Where  $A_c$  is the heating surface,  $T_{avg}$  denotes the average temperature of heating surface. The results indicate that, across all modes, the heat transfer coefficients of the TO and SC configurations remain generally consistent, with the TO configuration maintaining values approximately 400 higher than those of the SC configuration. Regarding temperature non-uniformity, the TO configuration also shows a marked improvement, effectively mitigating thermal stress within the cooling plate. Fig 12 depicts the thermal resistance of the two configurations under different operating modes. Thermal resistance is defined in Eq. (20), where  $T_{max}$  is the maximum coolant temperature,  $T_{in}$  is the coolant inlet temperature, and Q denotes the total external heat input. It quantifies the temperature rise associated with a unit heat flux. A smaller thermal resistance implies a smaller temperature difference required to transfer the same amount of heat, whereas a larger value may result in insufficient heat dissipation and heat accumulation. The results clearly demonstrate that the TO configuration exhibits superior thermal performance compared with the SC configuration.

$$R_{th} = (T_{max} - T_{in})/Q \tag{20}$$

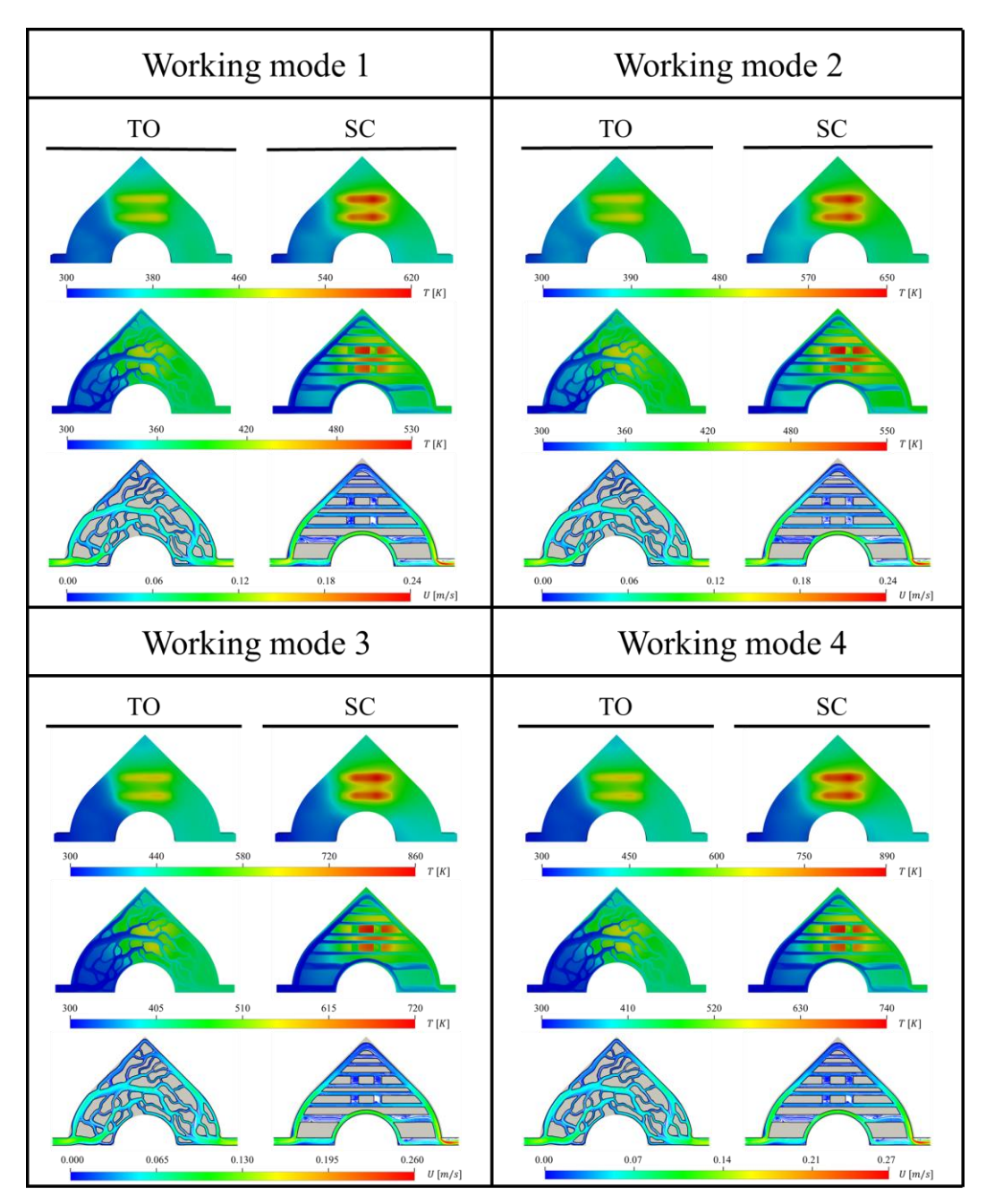


Fig 10. Temperature, velocity fields under different working modes

**Table 3.** Performance of two configuration under different working mode.

Working Mode	Configuration	$T_{ave}(K)$	$T_{max}(K)$	$\Delta p(Pa)$
Mode 1	ТО	354.7	512.6	36.8
	SC	363.1	590.3	46.9
Mode 2	ТО	366.6	534.3	34.7
	SC	376.5	619.3	44.6
Mode 3	ТО	391.4	682.5	32.6
	SC	407.4	818.7	43.1
Mode 4	ТО	402.6	703.1	31.1
	SC	420.5	847.2	41.5

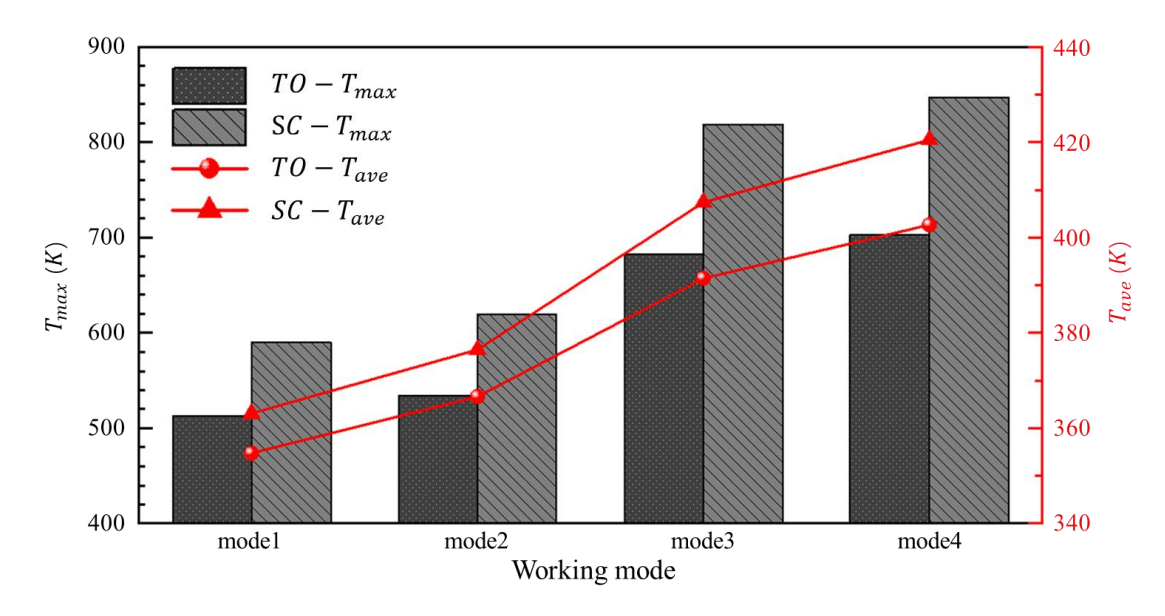


Fig 11. Heat transfer coefficient and temperature nonuniformity under different working modes

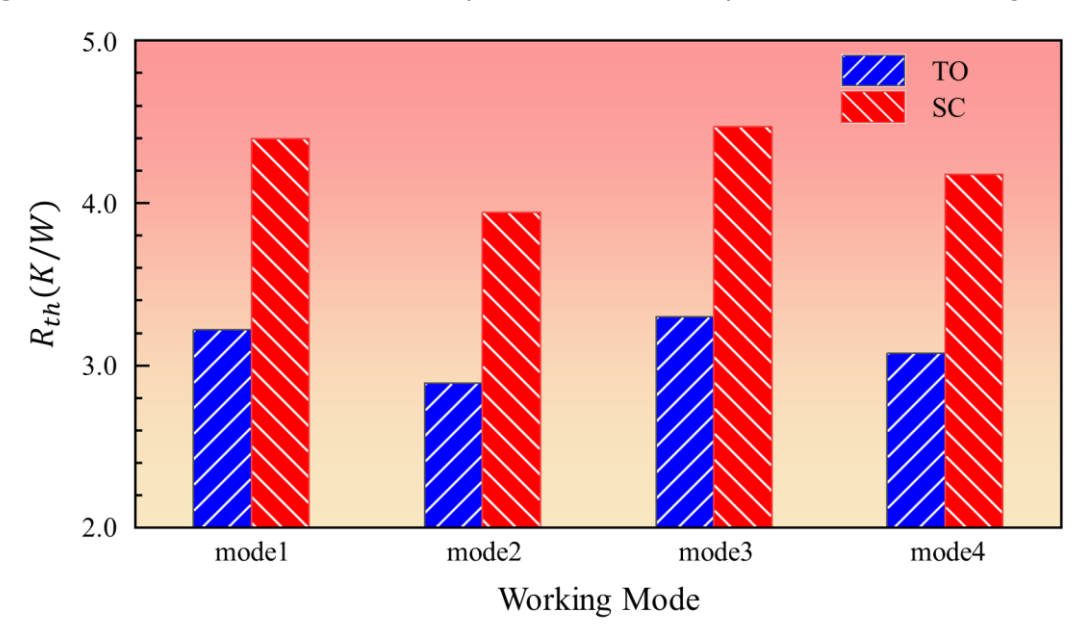


Fig 12. Thermal resistance under different working modes

To further analyze the temperature distribution characteristics of the coolant in the channels for both configurations under different working modes, the average coolant temperature at various angular cross-sections is extracted, as shown in Fig 13. Fig 14 depicts the angular variation of the average coolant temperature across the cross-sections of the two channels under different working modes.

In the SC configuration, the two configurations exhibit negligible temperature differences within the first 60°. As the angle approaches 70°, the average coolant temperature in the SC configuration rises sharply, reaching a peak near 80°. This peak is sustained temporarily, followed by an abrupt decline and then a gradual increase. A second sharp rise occurs around 100°, leading to the maximum temperature. Beyond this point, the average coolant temperature decreases, with pronounced oscillations after 150°. These temperature fluctuations are strongly influenced by the SC configuration geometry: the two distinct peaks originate from the vertical flow channels located in the motor's high-temperature source region, while the oscillatory behavior beyond 150° is attributed to the horizontal flow channels near the outlet.

In contrast, the TO configuration exhibits a gradual increase in average coolant temperature up to 120°, with only minor oscillations between 60° and 110°, and remains relatively stable thereafter. This

comparison indicates that the suboptimal configuration of the SC configuration leads to underutilization of a significant portion of the coolant, promoting flow convergence zones that cause localized overheating and reduced cooling efficiency. In contrast, the mesh-like structure of the TO configuration enhances coolant utilization, improves overall cooling performance, and markedly reduces temperature non-uniformity.

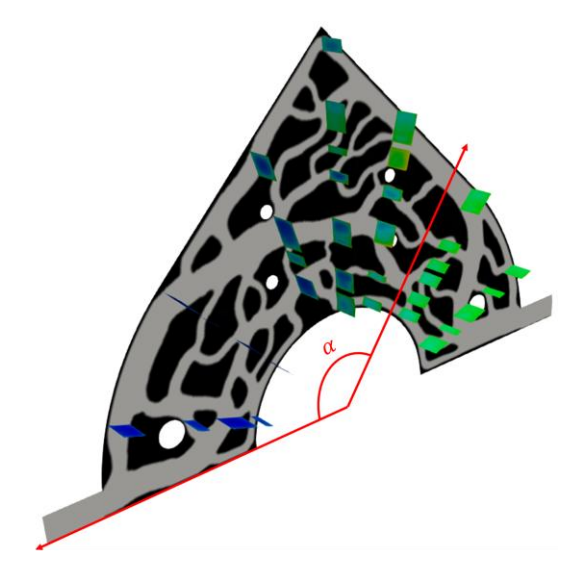


Fig 13. Schematic diagram of cooling plate slices

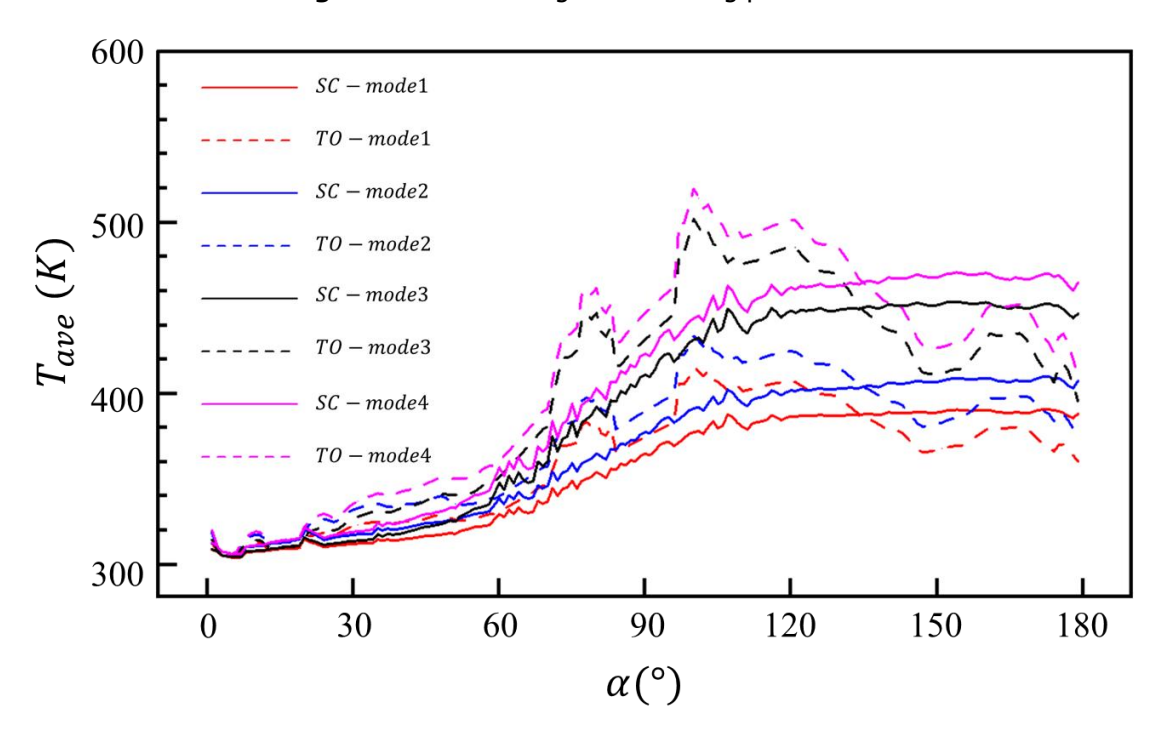


Fig 14. Variation of average coolant temperature with at different angular locations

#### 4. Conclusion

In this study, a multi-objective topology optimization is utilized to optimize the engine cooling plate with distributed heat sources. The optimization is conducted under constraints on volume and dissipated energy, with the objective of minimizing the average temperature in the design domain. Upon obtaining the optimized configuration, a reconstruction process is carried out, after which the optimized and conventional configurations are evaluated using numerical simulations. Furthermore, a series of thermal conditions were established to examine the robustness of the optimized configuration. The key conclusions are summarized as follows:

- (1) Compared with the conventional straight channel, the optimized channel distributes a larger portion of the coolant to the high heat-source regions, thereby reducing local hot-spot temperatures. The mesh-like sub-channels in the optimized configuration enlarge the fluid—solid contact area, enhance heat transfer efficiency, and ensure more uniform coolant distribution. In addition, the manifold design significantly increases coolant velocity within the channels, which reduces the boundary layer thickness and improves convective heat transfer. Moreover, the optimized configuration generates richer vortex structures than the conventional configuration, further promoting thermal exchange.
- (2) Based on practical operating conditions, different thermal environments were designed to evaluate performance. Under all tested conditions, the optimized configuration outperforms the conventional one. Specifically, the average temperature decreases by 2.31%, 2.63%, 3.93%, and 4.26% across the four operating modes, while the maximum temperature is reduced by 13.16%, 13.73%, 16.64%, and 17.01%, respectively. In addition, the pressure drop is lowered by 21.54%, 22.20%, 24.36%, and 25.10%. Moreover, the optimized configuration achieves a more uniform coolant temperature distribution and mitigates the formation of local convergence zones.

To sum up, the topology optimization cooling structures present superior flow and heat transfer performance, making it a promising tool for engineering applications.

#### References

- Gong, Y. & Xuejun, F. Supersonic combustion and hypersonic propulsion. Advances in Mechanics 43, 449-471 (2013).
- 2 Uyanna, O. & Najafi, H. Thermal protection systems for space vehicles: A review on technology development, current challenges and future prospects. Acta Astronautica 176, 341-356 (2020).
- 3 Yinhai, Z., Wei, P. & Ruina, X. Review on active thermal protection and its heat transfer for airbreathing hypersonic vehicles. Chinese Journal of Aeronautics 31, 1929-1953 (2018).
- 4 Luo, S., Xu, D., Song, J. & Liu, J. A review of regenerative cooling technologies for scramjets. Applied Thermal Engineering 190, 116754 (2021).
- Zhang, J., Zhang, S., Chunhua, W. & Xiaoming, T. Recent advances in film cooling enhancement: A review. Chinese Journal of Aeronautics 33, 1119-1136 (2020).
- ovan Foreest, A. et al. Transpiration cooling using liquid water. Journal of Thermophysics and Heat Transfer 23, 693-702 (2009).
- Glass, D. E., Dilley, A. D. & Kelly, H. N. Numerical analysis of convection/transpiration cooling. Journal of Spacecraft and Rockets 38, 15-20 (2001).
- 8 Li, B., Wang, W., Bei, S. & Quan, Z. Analysis of heat dissipation performance of battery liquid cooling plate based on bionic structure. Sustainability 14, 5541 (2022).
- 9 Fawaz, A., Hua, Y., Le Corre, S., Fan, Y. & Luo, L. Topology optimization of heat exchangers: A review. Energy 252, 124053 (2022).
- 10 Sun, C. et al. Thermal design of composite cold plates by topology optimization. International Journal of Mechanical Sciences 259, 108594 (2023).
- 11 Mekki, B. S., Langer, J. & Lynch, S. Genetic algorithm based topology optimization of heat exchanger fins used in aerospace applications. International Journal of Heat and Mass Transfer 170, 121002 (2021).
- 12 Li, X., Lu, Y., Wu, K. & Fan, X. in AIAA Propulsion and Energy 2019 Forum. 4302.
- 13 Li, X., Wu, K., Zhao, L. & Fan, X. Topology optimization of regenerative cooling structures under high Reynolds number flow with variable thermo-physical properties. Applied Thermal Engineering 258, 124602 (2025).
- 14 Li, X., Zhang, S., Qin, J. & Bao, W. Parametric analysis on the thermal behavior of cracking hydrocarbon fuel flow inside asymmetry heated cooling channels with micro-ribs. International Journal of Heat and Mass Transfer 160, 120154 (2020).

- 15 Olesen, L. H., Okkels, F. & Bruus, H. A high-level programming-language implementation of topology optimization applied to steady-state Navier-Stokes flow. International Journal for Numerical Methods in Engineering 65, 975-1001 (2006).
- 16 Yu, M. et al. Three-dimensional topology optimization of thermal-fluid-structural problems for cooling system design. Structural and Multidisciplinary Optimization 62, 3347-3366 (2020).
- 17 NLopt Algorithms. <a href="https://nlopt.readthedocs.io/en/latest/NLopt Algorithms/">https://nlopt.readthedocs.io/en/latest/NLopt Algorithms/</a>.
- 18 Lions J. Optimal Control of Systems Governed by Partial Differential Equations[M]. Springer, Berlin, Heidelberg, 1971.
- 19 Guest J K, Prévost J H, Belytschko T. Achieving minimum length scale in topology optimization using nodal design variables and projection functions[J]. International Journal for Numerical Methods in Engineering, 2004, 61(2): 238-254.
- Bourdin B. Filters in topology optimization[J]. International Journal for Numerical Methods in Engineering, 2001, 50(9): 2143-2158.
- Wang F, Lazarov B S, Sigmund O. On projection methods, convergence and robust formulations in topology optimization[J]. Structural and Multidisciplinary Optimization, 2011, 43(6): 767-784.